Antimicrobial Activity of Remineralizing Ion-Doped Amorphous Calcium Phosphates for Preventive Dentistry

*Lorenzo Degli Esposti[1], Andrei C. Ionescu[2], Francesca Carella[1], Alessio Adamiano[1], Eugenio Brambilla[2] and Michele Iafisco[1]**

[1]*Institute of Science and Technology for Ceramics, National Research Council, Faenza, Italy, [2]Oral Microbiology and Biomaterials Laboratory, Department of Biomedical, Surgical and Dental Sciences, University of Milan, Milan, Italy*

We have synthesized citrate-stabilized amorphous calcium phosphates doped with fluoride (F-ACP), strontium (Sr-ACP), and zinc (Zn-ACP) ions. ACP based materials were proven to have excellent remineralizing action on demineralized dental hard tissues while F^-, Sr^{2+}, and Zn^{2+} ions are known to have antimicrobial activity, so the aim of our work was to produce multipurpose materials for preventive dentistry that inhibit cariogenic bacteria and remineralize dental enamel and dentin. Doping ions were successfully incorporated into ACP up to 2 wt.% F^- and 12 wt.% Sr^{2+} or Zn^{2+} without altering ACP physical-chemical properties. Evaluation of viability of *Streptococcus Mutans* biofilm treated with ion-doped ACP materials showed that F-ACP and Sr-ACP have a direct inhibitory effect while Zn-ACP has a negligible effect. The different antibacterial activity was correlated to the ion-release properties of the materials, as in conditions mimicking a cariogenic environment F-ACP and Sr-ACP have a release of ca. 5–7% of total F^- or Sr^{2+} while only ca. 1% of total Zn^{2+} is released. All ion-doped ACP materials are able to remineralize *in vitro* demineralized human enamel slabs by epitaxial deposition of a new ion-doped crystalline phase in direct contact with the pristine one. Enamel slabs remineralized with F-ACP has an antibacterial/bacteriostatic action, proving that F-ACP acts as preventive antimicrobial agent. Overall, our work demonstrates the high potential of ACP doped with antibacterial ions for the preventive treatment of dental caries.

Keywords: dental remineralization, amorphous calcium phosphate, ion doping, antibacterial activity, *Streptococcus mutans*, antibacterial ion, fluoride, strontium

INTRODUCTION

According to the Global Burden of Disease study of 2017, dental caries is the most widespread non-communicable disease (James et al., 2018) which affects both industrialized and developing countries (Kassebaum et al., 2017). The disease results from an imbalance in the composition of the microorganisms, organized as biofilms, that permanently colonize any oral surface (Brambilla and Ionescu, 2021). It has been acknowledged that dysbiotic shifts in the composition of oral biofilm lead to the prevalence of acidogenic and acid-resistant species, such as *Streptococcus mutans* (Marsh and Zaura, 2017). These species feed with fermentable carbohydrates producing organic acids that lower the pH of the microenvironment on teeth surfaces (enamel and dentine), dissolving their

mineral component, hydroxyapatite (HA, $Ca_{10}(PO_4)_6(OH)_2$) (Selwitz et al., 2007). HA dissolution is referred to as the demineralization process and leads to the formation of dental cavities, which is a visible sign of the disease. The demineralization caused by cariogenic bacteria is amplified by dietary habits such as frequent intake of high amounts of sugar and other refined carbohydrates (Arheiam et al., 2020). Diets high in acidic food and drinks and diseases such as gastroesophageal reflux (GERD) contribute to the demineralization, both by direct activity and by exerting selection pressure towards acid-resistant, cariogenic species (Tahmassebi et al., 2006; Pace et al., 2008).

Modern dentistry is increasingly oriented towards early prevention of tooth decay rather than invasive restorative therapy. Preventive dentistry aims to stop the formation and progression of dental caries by promoting the remineralization of tooth surfaces and preventing factors causing dysbiotic shifts of the biofilm towards cariogenicity (Limeback, 2012). The first goal can be achieved using remineralizing agents, while the use of antimicrobial agents can lead to the second. Therefore, an ideal material for preventive caries treatment should show remineralizing capabilities and express antimicrobial activity against cariogenic biofilms.

The action of remineralizing agents is to restore the structure and preserve the mechanical properties of dental hard tissues (Cochrane et al., 2010). These materials favor the spontaneous teeth remineralization process induced by saliva. Saliva contains Ca^{2+} and PO_4^{3-}, the constituent ions of HA, that in physiological conditions deposit in the acid-eroded sites inducing regrowth of depleted dental enamel (Abou Neel et al., 2016). Remineralizing agents enhance this process by quickly delivering a significant amount of ions in the oral environment (Cochrane et al., 2010). Among such agents, calcium phosphate based materials are widely used as they contain the same constituent ions of HA and can release them in the oral environment (Roveri et al., 2009). One of the most promising agent for this application is amorphous calcium phosphate (ACP), as it has the highest degradability among the calcium phosphate phases. In this regard, we have recently developed a fluoride-doped amorphous calcium phosphate (F-ACP) stabilized by citrate ions that is able to crystallize into HA when in contact with enamel and dentine, thus showing a strong remineralizing activity (Iafisco et al., 2018).

In order to express solid antimicrobial activity, several oral healthcare products are used which contain antimicrobial agents such as chlorhexidine, fluoride, zinc, cetylpyridinium chloride (CPC), and other quaternary ammonium salts, SnF_2, and many other compounds (Miller et al., 1994; Franci et al., 2015; Chen et al., 2018). However, some of these agents have serious drawbacks; e.g., chlorhexidine and SnF_2 can induce permanent teeth staining (Addy and Moran, 1995), while the widespread use of CPC raises concerns about phenotypic adaptation or resistance by oral microbial strains (Mao et al., 2020). In the last decade, there was a rise in interest around the use of ions as antimicrobial agents (Chernousova

and Epple, 2013; Godoy-Gallardo et al., 2021). Antibacterial ions have the advantages of being simple to administer, cost-effective, and most importantly can be incorporated in the crystal lattice of human HA, conveying antibacterial or bacteriostatic effect to the dental surface (Lim et al., 2014; Helen and Kumar, 2019). Some of these ions can be used for HA doping, such as F^-, Sr^{2+}, and Zn^{2+}. The most important action of F^- is to prevent demineralization, as it leads to the formation of fluoride-doped HA, which is more resistant to acidic dissolution than pristine HA (Lynch et al., 2004). Fluoride ions were also proved to inhibit metabolic activity, particularly in cariogenic bacteria, thus reducing acid production (Hamilton, 1977; Yoon and Newman, 1980; Barbier et al., 2010). The antibacterial activity of Sr^{2+} is significant yet less apparent, and its mechanism of action has not been fully elucidated (Brauer et al., 2013). Zn^{2+} is an essential oligoelement (i.e., at low concentrations) that has been proven toxic towards bacteria when provided at high concentrations. It is thought that the toxic effect of Zn^{2+} is due to competition with other metals for metal-binding proteins, resulting in protein malfunction and bacterial metabolism disruption (Blencowe and Morby, 2003; Godoy-Gallardo et al., 2021).

A preventive approach towards dental decay would benefit from the use of multifunctional materials able to remineralize the damaged mineral phase and to show antimicrobial activity against cariogenic bacteria at the same time. Previous works have proved that ACP doped with fluoride, silver, gallium, and zinc can inhibit several bacteria strains (Zhao et al., 2013; Yang et al., 2017; Cao et al., 2020). However, the effect of antibacterial ACPs has only been addressed once (Yang et al., 2017), and to the best of our knowledge, the doping of ACP with F^- and Sr^{2+} to obtain an antibacterial effect has never been reported. In addition, there are no works that have studied the bacteriostatic effect of enamel surface upon remineralizion with ACP.

On the base of these premises, the aim of this work was 1) to produce citrate-stabilized ACPs doped with F^-, Sr^{2+}, and Zn^{2+} ions, 2) to evaluate their antibacterial activity, remineralization ability, and influence of enamel-treated surfaces on biofilm formation, and 3) to correlate these caries preventing activities with the ion release and HA formation in conditions that mimic the carious environment. First, the following materials were prepared: 1) non-doped citrate-stabilized ACP to act as negative control (ACP), 2) fluoride-doped ACP containing 2 wt% F^- (F2-ACP), 3) ACPs doped with ca. 6 and 12 wt.% Sr^{2+} (Sr6-ACP and Sr12-ACP, respectively), and 4) ACPs doped with ca. 6 and 12 wt.% Zn^{2+} (Zn6-ACP and Zn12-ACP, respectively). These materials were extensively characterized and afterward, their antibacterial activity was tested against *S. mutans* biofilms evaluating their action as direct inhibitory effect and induced inhibitory effect on demineralized human enamel remineralized using these compounds. The antibacterial activity was tested under normal or enhanced cariogenic conditions controlled by sucrose addition. Finally, we studied the occurring ion release and the dissolution/crystallization of the ACP compounds under conditions mimicking those employed in the antibacterial tests.

MATERIALS AND METHODS

Materials

Calcium chloride dihydrate ($CaCl_2 \cdot 2H_2O$, ≥99.0% pure), hydrochloric acid (HCl, ≥37.0% pure), lactic acid ($C_3H_6O_3$, ≥88.0% pure), modified Dulbecco's phosphate-buffered saline (PBS, without $CaCl_2$ and $MgCl_2$), orthophosphoric acid (H_3PO_4, ≥85% pure), sodium carbonate monohydrate ($Na_2CO_3 \cdot 2H_2O$, ≥99.0% pure), sodium citrate tribasic dihydrate ($Na_3(C_6H_5O_7) \cdot 2H_2O$, ≥99.0% pure), sodium fluoride (NaF, ≥99.0% pure), sodium lactate solution ($NaC_3H_5O_3$, ≥50.0% pure), sodium phosphate dibasic dihydrate ($Na_2HPO_4 \cdot 2H_2O$, ≥99.0% pure), strontium chloride hexahydrate ($SrCl_2 \cdot 6H_2O$, ≥99.0% pure), zinc chloride ($ZnCl_2$, ≥98.0% pure), were purchased from Sigma Aldrich (St. Luis, MO, United States). Reagents, culture media, and disposables used for the microbiological procedures and viable biomass assay were obtained from E. Merck AG (Darmstadt, Germany).

Sample Preparation

ACP and ion-doped ACP materials were synthesized as reported by Iafisco et al. (2018) with some modifications. ACP was prepared by mixing at room temperature equal volumes of two aqueous solutions, consisting in (A) 0.100 M $CaCl_2$ + 0.100 M $Na_3(C_6H_5O_7)$ and (B) 0.120 M Na_2HPO_4 + 0.200 M Na_2CO_3. After mixing, the pH was brought to 8.5 with concentrated HCl. After 60 s of mixing, the precipitated particles were collected by centrifugation (7,000 rpm, 4°C, 5 min), repeatedly washed with ultrapure water, and freeze-dried. For ion-doped ACPs, the concentration of precursor salts (NaF, $SrCl_2$, and $ZnCl_2$), necessary for achieving the doping of 2 wt. % for fluoride and 6 or 12 wt. % for zinc and strontium was obtained through chemical reaction optimization performing multiple syntheses (data not shown). Finally, F2-ACP was prepared with the same procedure reported above and the addition of 0.070 M NaF to solution (B). Sr6-ACP and Sr12-ACP were prepared with the same procedure with the addition of, respectively, 0.0125 or 0.025 M $SrCl_2$ to the solution (A). Similarly, a total of 0.010 or 0.018 M of $ZnCl_2$ were added to the solution (A) for preparing Zn6-ACP and Zn12-ACP, respectively.

Chemical, Morphological and Structural Characterization

Powder X-Ray Diffraction

PXRD patterns of the samples were recorded on a D8 Advance diffractometer (Bruker, Karlsruhe, Germany) using Cu Kα radiation generated at 40 kV and 40 mA. PXRD patterns were collected in the 10–60° 2θ range with a step size of 0.02° and a collection time of 0.5 s.

Fourier Transform Infrared Spectroscopy

FT-IR spectra were collected on a Nicolet 5,700 spectrometer (Thermo Fisher Scientific Inc., Waltham, MA, United States) in transmission mode by accumulating 32 scans in the range between 4,000 and 400 cm^{-1} with a resolution of 2 cm^{-1} using the KBr pellet method.

Elemental Analysis

Ca and P contents of the samples were measured by inductively-coupled plasma optical emission spectrometry (ICP-OES) using an Agilent 5,100 instrument (Agilent Technologies, Santa Clara, CA, United States), while F content was measured with an Intellical ISEF121 ion-selective electrode for fluoride (ISEF) (Hach Lange, Loveland, CO, United States). 10 mg of the powdered samples were dissolved in 50 mL of a 1 wt.% HNO_3 aqueous solution for both analyses. Standard fluoride solutions were prepared from a certified standard (1,000 ppm F certified standard, Sigma Aldrich, St. Luis, MO, United States) in the same acidic medium; the calibration curve was then obtained by analyzing the standard solutions on the same day they were prepared.

Antibacterial Tests and Remineralization Test

Bacteria

A pure suspension of *S. mutans* strain ATCC 35668 was obtained as follows. Mitis Salivarius Bacitracin agar (MSB agar) plates were inoculated with the *S. mutans* strain and incubated aerobically in a 5% CO_2-supplemented atmosphere at 37°C for 48 h. A pure culture was obtained after transferring an inoculum in Brain Heart Infusion (BHI) broth and further incubating in a 5% CO_2-supplemented atmosphere at 37°C overnight. Cells were harvested by centrifugation (2,200 × g, 19°C, 5 min), washed twice with sterile phosphate-buffered saline (PBS), and resuspended in the same buffer. The suspension was sonicated using low-energy output (7W for 30 s, B-150 Sonifier, Branson, Danbury, CT, United States) to disperse bacterial chains. Finally, the suspension was adjusted to an optical density of 1.0 on the McFarland scale, corresponding to a concentration of approximately 6.0 × 10^8 cells/mL.

Antibacterial Tests

Each well of a 96-well plate was inoculated with 20 μL of the *S. mutans* suspension. Then, half of the wells were added with 200 μL of BHI containing 0.2 wt.% dextrose (S-), while 200 μL of BHI additioned with 5 wt.% of sucrose (S+) was placed into the other half. The latter medium favored bacterial metabolism and acid production, increasing the cariogenic challenge. The plate was incubated in a 5% CO_2-supplemented atmosphere at 37°C for 24 h to form a multilayered biofilm. Then, the supernatant was carefully discarded by pipetting, and the wells were washed twice with sterile PBS to remove non-adherent cells. Each ACP was made into a slurry by mixing 1:3 w/v with ultrapure water, stored at 37°C for 24 h, vortexed, then a total of 50 μL of the slurry was inserted in each well. A total of 6 wells were used for each slurry under each medium (S-/S+). Additional wells (n = 6 for each medium) were inoculated with sterile PBS to be negative controls. After a contact time of 1h, the supernatant slurry was gently discarded, and the wells were washed twice with sterile PBS. The

amount of viable and metabolically active biomass in each well was determined using the MTT assay, as explained below.

Substrate

A total of 60 human teeth extracted for clinical reasons (before the COVID-19 outbreak) were obtained and stored at −20°C until use. The Institutional Review Board of the University of Milan approved the protocol (codename: SALTiBO-2017). Each donor signed informed consent in a written form. All *in vitro* experiments were performed following the Declaration of Helsinki, updated by the World Medical Association in 2013. Enamel disks (6.0 mm in diameter and 1.5 mm thick) were cut from the teeth surfaces using a custom-made water-cooled diamond trephine bur (Indiam, Carrara, Italy). A total of 105 enamel disks were prepared for the study, using this procedure to obtain more than one disk from each tooth. All surfaces were polished using silicon carbide paper (600 and 1,200 grit), and the surfaces were etched with a 37 wt.% H_3PO_4 solution for 30 s, followed by extensive rinsing with water. Specimens were then randomly divided into 7 treatment groups ($n = 15$). Each ACP material was made into a slurry by mixing 1:3 w/v with ultrapure water, and the enamel disks from each group were immediately dipped into the corresponding slurry, brushed for 3 min using a disposable microbrush, then stored at 37°C for 24 h. The seventh group was dipped in Dulbecco's PBS (no remineralization occurring) and was used as the negative control.

After storage, specimens were rinsed for 2 min with Dulbecco's PBS to detach the slurry, then air-dried in a laminar flow cabinet.

Bioreactor

The bioreactor used in the present study was a previously described modification (Ionescu et al., 2018) of a commercially available drip-flow reactor (DFR 110, BioSurface Technologies; Bozeman, MT, United States). The modified design allowed customized PTFE trays to be placed on the bottom of the flow cells to submerge the disks' surfaces in the flowing medium. A total of 12 specimens from each treatment group were randomly divided into the flow cells of the bioreactor (4 flow cells, $n = 3$ disks/cell from each group). The bioreactor and its tubing together with the treated disks were then sterilized using a chemical peroxide-ion plasma sterilizer (Sterrad, ASP, Irvine, CA, United States) that reached a maximum temperature of 45°C, thus preventing heat-related alterations of the disks' surfaces.

The bioreactor was assembled inside a sterile hood, and each flow cell was inoculated with 10 mL of the *S. mutans* suspension to allow bacterial adherence. After 4 h, a peristaltic pump (RP-1k; Rainin, Emeryville, CA, United States) provided a constant flow of medium through the flow cells (9.6 mL/h) for 20 h. Half of the flow cells ($n = 6$ disks/group) were flowed with BHI (S-), while the other half ($n = 6$ disks/group) were flowed with BHI additioned with 5 wt.% of sucrose (S+).

Viable Biomass Assessment

Viable and metabolically active biomass adherent to the specimen surface was assessed using a tetrazolium-based assay. In brief, a tetrazolium salt stock solution was prepared by dissolving 5 mg/mL 3-(4,5-dimethylthiazol-2-yl-2,5-diphenyltetrazolium bromide (MTT) in sterile PBS; a phenazinium salt stock solution was prepared by dissolving 0.3 mg/mL of N-methylphenazinium methyl sulfate (PMS) in sterile PBS. The solutions were stored at 2°C in light-proof vials until the day of the experiment when a fresh measurement solution (FMS) was prepared by diluting 1:10 v/v of MTT stock solution and 1:10 v/v of PMS stock solution in sterile PBS. A lysing solution (LS) was prepared by dissolving 10% v/v of sodium dodecyl sulfate (SDS) and 50% v/v dimethylformamide in distilled water and stored at 2°C until the day of the experiment when it was warmed at 37°C for 2 h before use. In the antibacterial experiment, a total of 100 μL of FMS was pipetted into each well of the 96-well plate. After the specified incubation time, the medium flow through the bioreactor was halted, flow cells opened, the disks were carefully removed and immediately placed into Petri plates containing sterile PBS at 37°C. They were gently washed three times with sterile PBS to remove non-adherent cells and finally placed inside the wells of two 48-well plates containing 300 μL of FMS each. The plates from all microbiological experiments were then incubated at 37°C under light-proof conditions for 1 h. During incubation, electron transport across the microbial plasma membrane and, to a lesser extent, microbial redox systems converted the yellow salt to insoluble purple formazan crystals. The intermediate electron acceptor (PMS) facilitated the conversion at the cell membrane level. The unreacted FMS was gently removed by aspiration, and the formazan crystals were dissolved by adding 120 μL (96-well plate) or 300 μL (48-well plates) of LS to each well. The plates were stored for an additional hour under light-proof conditions at room temperature; 100 μL of the solution from each well was then transferred into new 96-well plates. The absorbance of the solution was measured using a spectrophotometer (Genesys 10-S, Thermo Spectronic, Rochester, NY, United States) at a wavelength of 550 nm; results were expressed as relative absorbance in optical density (OD) units corresponding to the amount of adherent, viable and metabolically active *S. mutans* biomass.

Ion Release and Structural Characterization After Incubation as Slurry

To mimic the conditions of antibacterial activity tests, ACPs were incubated in aqueous slurries at pH 7.0 and 4.5, representing the standard and cariogenic conditions, respectively. In detail, 200 mg of ACP dry powder were put in sealed 2 mL Eppendorf vials together with 600 μL of ultrapure water (pH 7.0) or 0.1 M lactate buffer (pH 4.5) in triplicate and incubated at 37°C for 24 h. Afterward, the slurries were washed with 10 mL of the same buffer and the powders were collected by centrifugation (7,000 rpm, 4°C, 5 min) and freeze-dried. ICP-OES and ISEF were used to quantify ACPs ion release during incubation as slurry. In detail, 0.5 mL of the supernatants were mixed with 0.2 mL of HNO_3 and brought to 10 mL with water before the analysis.

PXRD and FT-IR of the dried samples after incubation as slurry were performed as reported above. FT-IR spectra were further processed to highlight the specific peaks associated with
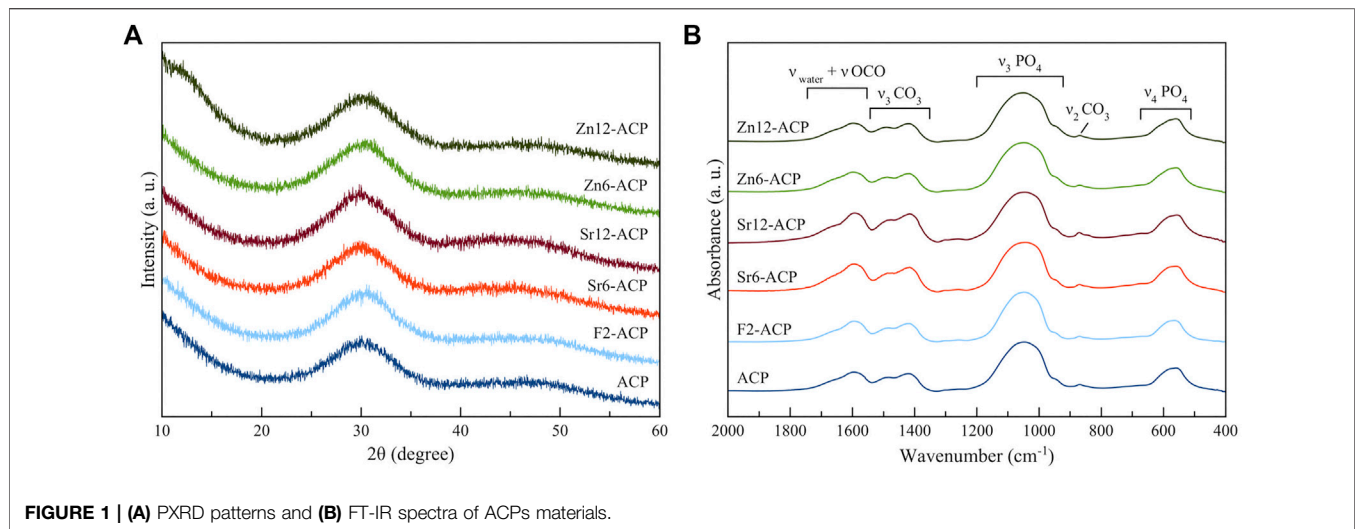
FIGURE 1 | (A) PXRD patterns and **(B)** FT-IR spectra of ACPs materials.

ACP and HA in the samples. In detail, the second derivative of the spectra using MagicPlotPro software was calculated by applying the Savitzky–Golay algorithm after spectra smoothing to improve the signal-to-noise ratio. The second derivative of spectra was inverted to show the negative peaks.

Scanning Electron Microscopy and Energy-Dispersive X-ray Spectroscopy

Energy dispersive X-ray spectra (SEM-EDS) and SEM images of both the ACP materials and the ACP-treated enamel disks were collected using a tabletop scanning electron microscope (TM4000Plus, Hitachi, Schaumburg, IL, United States) equipped with an EDS probe (Q75, Bruker, Berlin, Germany). After 24 h of storage, the slurry of the ACP and the enamel disks (n = 3/group) were dried overnight in the vacuum bell and then placed in the observation chamber of the SEM. Specimens were observed in surface-charge reduction mode without sputter-coating, using an accelerating voltage of 15 kV and a maximum magnification of 5,000× in secondary electron and backscattered electron mode. Three randomly selected fields were acquired for each specimen at ×200 magnification in full-frame mode using an acquisition time of 150 s. Acquired data represented the elemental composition of the ≈1 μm superficial layer.

Statistical Analysis

All analyses were performed in triplicate. Results are provided as means ±1 standard deviation. For the microbiological analyses, statistics were performed using JMP 10.0 software (SAS Institute, Cary, NC, United States). Normal distribution of data was checked using Shapiro–Wilk's test, and homogeneity of variances was verified using Levene's test. Means and standard errors were calculated from the viable biomass raw data. A two-way analysis of variance (ANOVA) was employed, considering "ACP materials" and "culture medium" as fixed factors. Tukey's test was applied for post-hoc analyses. The level of significance (α) was set to 0.05.

RESULTS AND DISCUSSION

Structural and Compositional Characterization of Ion-Doped ACPs

PXRD analysis (**Figure 1A**) shows that all ACP materials are amorphous as no diffraction peaks are present. Instead, only a broad band centered at 30° 2θ can be observed, which is characteristic of amorphous calcium phosphate (Iafisco et al., 2018). This suggests that Zn^{2+} and Sr^{2+} doping does not induce ACP crystallization to HA when it is stabilized by citrate, similarly to what was previously demonstrated for F^- doping (Iafisco et al., 2018). Indeed, our previous works have proven that citrate can stabilize ion-doped ACP and preserve its amorphous nature in dry state even for several years (Iafisco et al., 2018; Degli Esposti et al., 2021).

The amorphous nature of the materials is confirmed by their FT-IR spectra (**Figure 1B**). In fact, the main phosphate vibrational bands at ca. 1,050 and 600 cm^{-1}, corresponding respectively to $\nu_3 PO_4$ and $\nu_4 PO_4$ modes, are broad and convoluted, as typical features for non-crystalline calcium phosphate phase (Combes and Rey, 2010). In addition, all samples present bands associated to carbonate ions at 870 cm^{-1} and at 1,420–1,490 cm^{-1}, corresponding respectively to $\nu_2 CO_3$ and $\nu_3 CO_3$ vibrations, and bands related to νOCO vibration of citrate ions at 1,585 and 1,630 cm^{-1} together with the band of water at ca. 1,650 cm^{-1}. The intensity of these bands is similar for almost all samples, suggesting a comparable content of citrate and carbonate ions. The sole exceptions are the Sr-doped ACPs that have slightly more intense bands, suggesting a marginally higher citrate and carbonate content which is induced by the presence of Sr^{2+} ions (**Supplementary Figure S1**). This finding is in accordance with previous observations for Sr-doped HA (Li et al., 2007; Iafisco et al., 2014) where it has been proposed that the strain of the HA structure due to the accommodation of bigger Sr^{2+} ions in substitution to smaller Ca^{2+} leads to an incremented carbonate incorporation. A similar mechanism could occur for

TABLE 1 | Chemical composition of the ion-doped ACP materials.

Sample	Ca (wt. %)	P (wt. %)	F (wt. %)	Sr (wt. %)	Zn (wt. %)	Cations/P (mol)
ACP	28.8 ± 0.3	13.1 ± 0.2	-	-	-	1.69 ± 0.01
F2-ACP	30.0 ± 1.0	13.0 ± 0.2	2.3 ± 0.1	-	-	1.79 ± 0.01
Sr6-ACP	23.1 ± 0.4	11.6 ± 0.2	-	6.5 ± 0.1	-	1.74 ± 0.01
Sr12-ACP	17.9 ± 0.3	9.9 ± 0.2	-	9.9 ± 0.1	-	1.76 ± 0.01
Zn6-ACP	23.2 ± 0.6	12.6 ± 0.3	-	-	6.4 ± 0.2	1.67 ± 0.01
Zn12-ACP	20.4 ± 0.6	13.3 ± 0.4	-	-	12.9 ± 0.4	1.65 ± 0.01

ACP, as it is structurally similar to HA (Posner and Betts, 1975).

The chemical composition of the samples is reported in **Table 1**. The quantity of Sr^{2+}, Zn^{2+}, and F^- are present in the materials at doping levels close to the desired values which are 6 wt.% and 12 wt.% for Sr^{2+} and Zn^{2+} and 2 wt% for F^-. Both doping with Sr^{2+} and Zn^{2+} involves a decrease of calcium content, suggesting a cationic substitution in the ACP structure. The doping through substitution mechanism is proved also by the values of molar ratios (Ca + Sr or Zn)/P which remain almost constant (1.65–1.74) and close to the value of undoped ACP (1.69). On the other hand, F2-ACP has a slightly higher Ca/P ratio (1.79) due to the fact that fluoride ions, as previously found, lead to a higher calcium content (Iafisco et al., 2018).
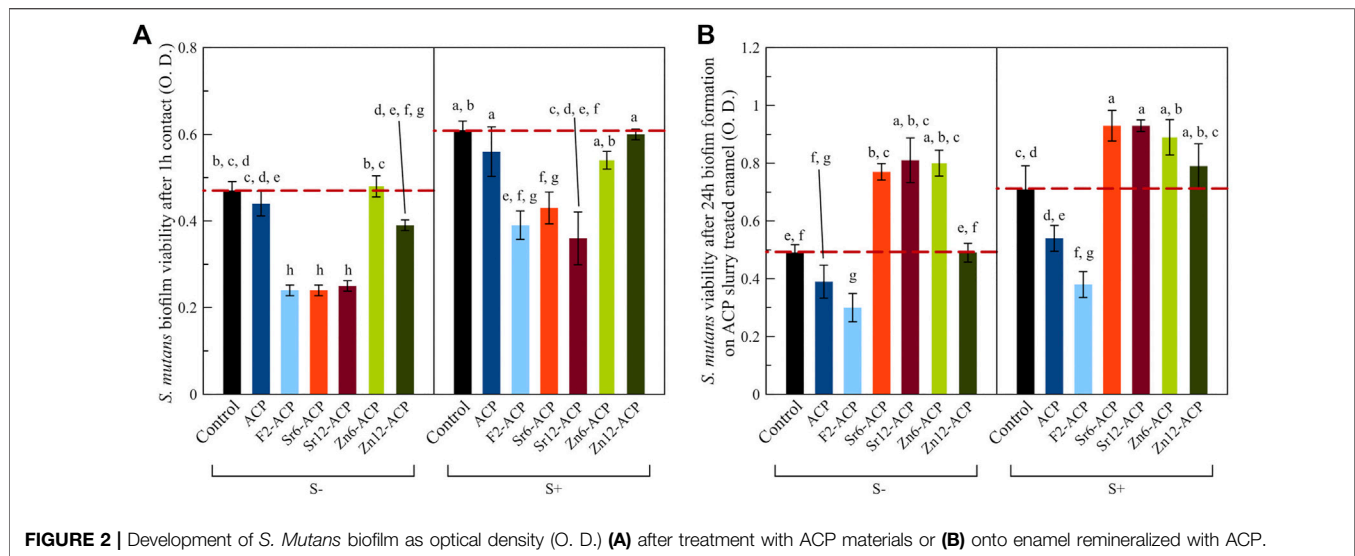
Antibacterial and Remineralizing Activity of Ion-Doped ACPs

The antibacterial activity of ion-doped ACP materials was evaluated against an *S. Mutans* biofilm. As a first test, the antibacterial activity of a concentrated suspension (slurry) of ACPs directly administered on a fully-developed bacterial biofilm was evaluated. Most remineralizing compounds are provided to the oral environment in formulations that are activated when diluted with the water contained in the saliva, allowing for the conversion of metastable calcium phosphate compounds into HA on teeth surfaces. Therefore, an aqueous slurry of ACPs (200 mg of powder in 600 μL of water) was prepared and left to react at 37°C for 24 h. These experimental conditions were also previously used to prove the remineralizing action of ACP (Iafisco et al., 2018). Then, the slurry was administered to an *S. Mutans* biofilm.

It is known that, in the oral environment, microorganisms are organized into biofilms that provide the means to survive and thrive on teeths' hard surfaces while, at the same time, providing shelter against antimicrobial agents. Furthermore, biofilms can select the ionic species that can be accumulated inside themselves, directly influencing the dissolution rate of the hard tissues or showing enhanced resistance against antimicrobial ions such as fluoride (Ionescu et al., 2019). The test was performed both in the absence (S-) or presence (S+) of 5 wt.% sucrose added to the culture medium. The latter condition provides bacteria with the substrate to increase their metabolic activity, resulting in increased acid production and thus cariogenicity, causing an additional drop in pH values from about 5.5. to below 4.0 in the static bioreactor model. The same drop occurs in the oral environment after sugar intake. The viable and metabolically

active biomass in the biofilm after ACPs treatment is reported in **Figure 2A**. Both ACPs and culture medium factors are highly significant ($p < 0.0001$), and the interaction between them is at the significance limit ($p = 0.0415$), meaning that, to some extent, sucrose addition influenced the biofilm response to the different ACP materials. ACP shows no inhibitory effect in both media. On the other hand, F2-ACP, Sr6-ACP, and Sr12-ACP show a highly significant inhibitory effect against the biofilm both with S- and S+ media ($p < 0.01$), with 51, 51, and 53% viability for F2-ACP, Sr6-ACP, and Sr12-ACP respectively in S- biofilms, and 64, 70, and 59% viability in S+ biofilms. Therefore, these materials have similar efficacy, irrespective of the doping content, suggesting that low doping levels can already provide the highest antibacterial effect. Interestingly, Zn6-ACP and Zn12-ACP samples show no antibacterial activity compared to the control or non-doped ACP, both in S- and S+ biofilms.

Afterward, the antibacterial activity of ACPs as preventive agents was evaluated. In this case, the aqueous slurry of the ACP materials were used to remineralize enamel slabs before evaluating biofilm formation under S- and S+ media. This approach is the closest way to reproduce *in vitro* the clinical situation where teeth with initial demineralization are treated with a remineralizing compound and oral biofilm steadily re-colonizes treated surfaces. In this case, the use of a bioreactor is of utmost importance in reproducing the oral environment (Ionescu and Brambilla, 2021). In the present study, both ACPs and culture medium factors are highly significant ($p < 0.0001$), yet the interaction between them is not significant ($p = 0.1136$), meaning that the growth conditions did not influence the biofilm response to the different ACP materials. F2-ACP induced a significant antibacterial effect both in S- and S+ conditions, with 61% viability for S- biofilms and 54% viability for S+ biofilms ($p < 0.0001$ compared to the control, untreated enamel, and $p < 0.05$ compared to non-doped ACP-treated substrate, **Figure 2B**). The biofilm growth on enamel slabs treated with Zn^{2+} or Sr^{2+}-doped ACP is comparable to the negative control or even higher. This finding suggests that the deposition of a fluoride-rich layer on enamel imparts an antibacterial/bacteriostatic effect, while for the other tested ACP materials this preventive effect is not reached. The reason for this behavior may be due to a reduced release of Sr^{2+} or Zn^{2+} ions from the surface layer or an increased buffering effect of such layer towards biofilm's acidogenicity. In fact, the relative increase in biomass viability of Zn^{2+} or Sr^{2+}-doped ACP compared to the control was lower when the biofilm was more acidogenic, and its metabolism was increased, supporting the

FIGURE 2 | Development of *S. Mutans* biofilm as optical density (O. D.) **(A)** after treatment with ACP materials or **(B)** onto enamel remineralized with ACP.

hypothesis of a buffering effect being reduced in the presence of increased acid production. The pH of the supernatant FMS after removal of enamel and bacteria (**Supplementary Figure S2**) is strongly dependent on the growth conditions, as in S- is around 5.0–5.4 while in S+ ranges 4.5–4.8 due to the incremented acidogenic activity of *S. Mutans* supplemented with sucrose. Overall, the presence of enamel leads to slightly higher pH values both in S- and S+ due to the buffering effect of phosphate ions released by enamel HA, but there are no statistically significant differences between enamel and enamel treated with ACP samples.

Enamel disks treated with the tested ACP materials were examined using SEM-EDS to confirm their remineralization (**Figure 3**). EDS spectra showed that non-doped ACP-treated surfaces had a similar composition to pristine enamel. The doped ACP materials deposited on the surface relevant amounts of their respective doping elements. Interestingly, F and Sr surface content was ≈1 wt% independently from the amount of ion doping of the ACP. Zn content was ≈1.75 and ≈2.5 wt. % for disks treated with Zn6-ACP and Zn12-ACP, respectively. All these values were much lower than those contained in the ACP materials. This finding suggests that enamel surfaces can only absorb a finite amount of these doping ions during the tested treatment time (24 h). This result helps explain the microbiological behavior of the treated enamel disks, where similar biofilm formation was found independently from the doping ion content, and only fluoride doping was responsible for a significant decrease in the viability of the biomass.

Two SEM acquisition modes (secondary electrons and backscattered electrons) allowed to gather information at different depths on the material. Backscattered electrons mode is sensitive to differences in the atomic number of the specimen, thus providing topographical information about its composition. However, the depth of interaction of backscattered electrons (≈1 μm at 15 KV) is always about two orders of magnitude deeper than that of the secondary electrons. Collecting both types of electrons allows obtaining information on the

crystallization of the remineralized layer and its surface morphology, such as the evenness of the deposited layer. After the demineralization procedure, negative control enamel disks showed the prismatic structure made by native HA crystals that constitute the primary enamel prisms unit, as etching procedures dissolved the superficial amorphous layer. A demineralization pattern was identified, mainly dissolving the less crystalline interprismatic mineral phase. The storage solution, only containing phosphate ions, did not remineralize enamel structures. On the contrary, all tested ACP materials showed remineralization features (**Figure 3**). Through comparison of control and treated specimens, it is evident that the application of the materials for 24 h has led to the remineralization of the etched enamel by depositing a new crystalline phase in direct contact with the pristine one. Epitaxial growth of nanocrystallites was identified and was found to be most pronounced in Zn12-ACP followed in order of magnitude by Sr12-ACP and F2-ACP.

These observations indicate that the amount of ions by which citrate-stabilized ACP materials were doped had a significant and positive effect on remineralization, while biofilms were relatively insensitive to differences in the amount of Sr^{2+} and Zn^{2+} ions, while for F2-ACP even a small amount of F^- imparts an antibacterial effect.

Crystallization and Ion Release of ACPs After Incubation as an Aqueous Slurry
The antibacterial activity of ACP materials was correlated with their ion release capability. Therefore, slurries of ACP samples were maintained at pH 7.0 or at pH 4.5 (to mimic the condition occurred in presence of *S. Mutans* and sucrose) at 37°C for 24 h.

The amount of ions released from the ACP materials (expressed as percentage of the total amount) is reported in **Table 2**. Overall and not surprisingly, the amount of ions released is higher at pH 4.5 than at pH 7.0 for every ACP material. Indeed, this pH-dependency is in agreement with
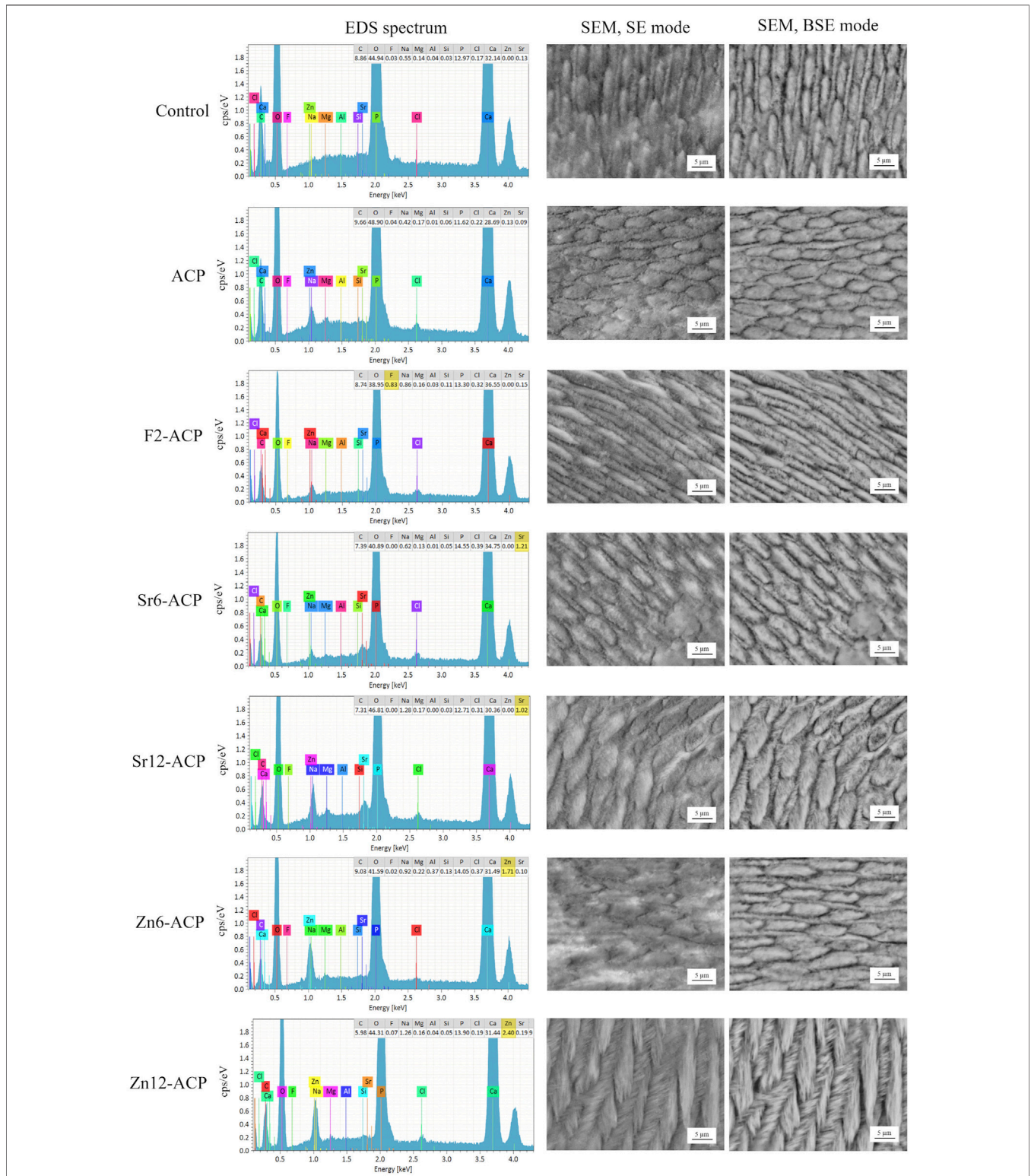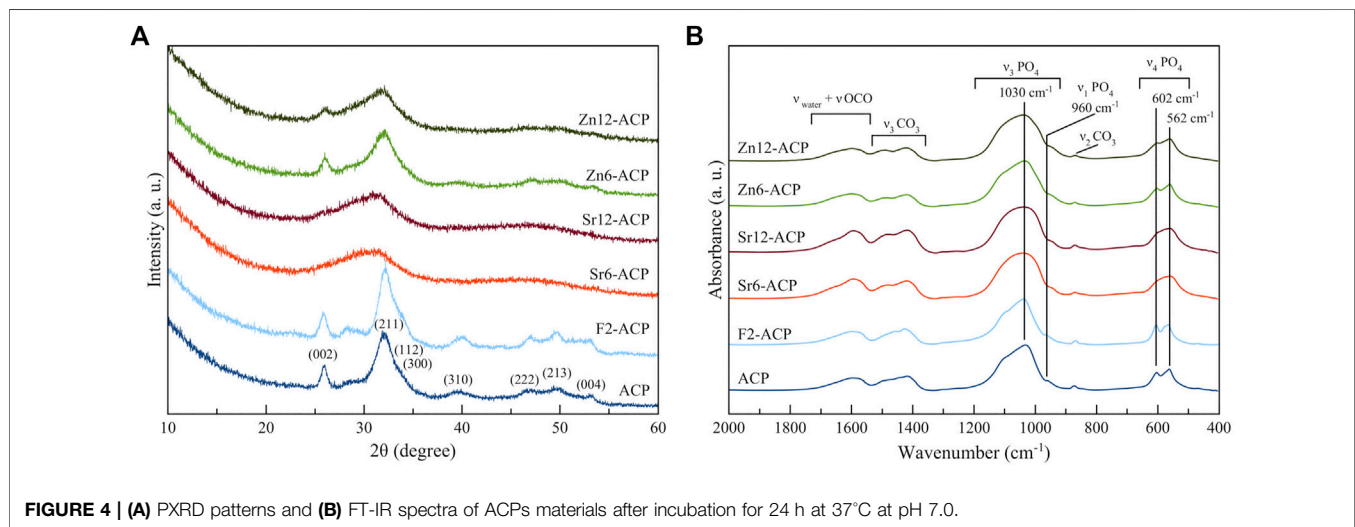
FIGURE 3 | EDS spectra and SEM micrographs of demineralized human enamel (control) and enamel surfaces treated with ACP materials for 24 h. The composition of pristine enamel surfaces indicates the presence of magnesium- and carbonate-doped HA together with sodium chloride. Shallow traces of aluminum and silicon were sometimes detected as a consequence of polishing procedures. ACP-treated surfaces showed a very similar spectrum to that of pristine enamel. Enamel surfaces treated with the ion-doped ACP compounds clearly showed the peaks corresponding to the doping element, yet the normalized wt. % of the doping element was much lower and did not increase when its presence was twice as much in the ACP compound. Next to each EDS spectrum is a corresponding SEM micrograph at ×5,000 magnification acquired in secondary electrons mode and in backscattered electrons mode. Both Zn12-ACP and Sr12-ACP showed the presence of a compact layer of crystallites with epitaxial growth remineralizing enamel structures. F2-ACP and non-doped ACP showed a layer made by smaller cristallites without a defined orientation.

TABLE 2 | Amounts of ions released by ACP samples under neutral and acidic pH conditions, as assessed by ICP-OES and ISEF. The acidic conditions reproduce the challenge of a metabolically active, cariogenic biofilm.
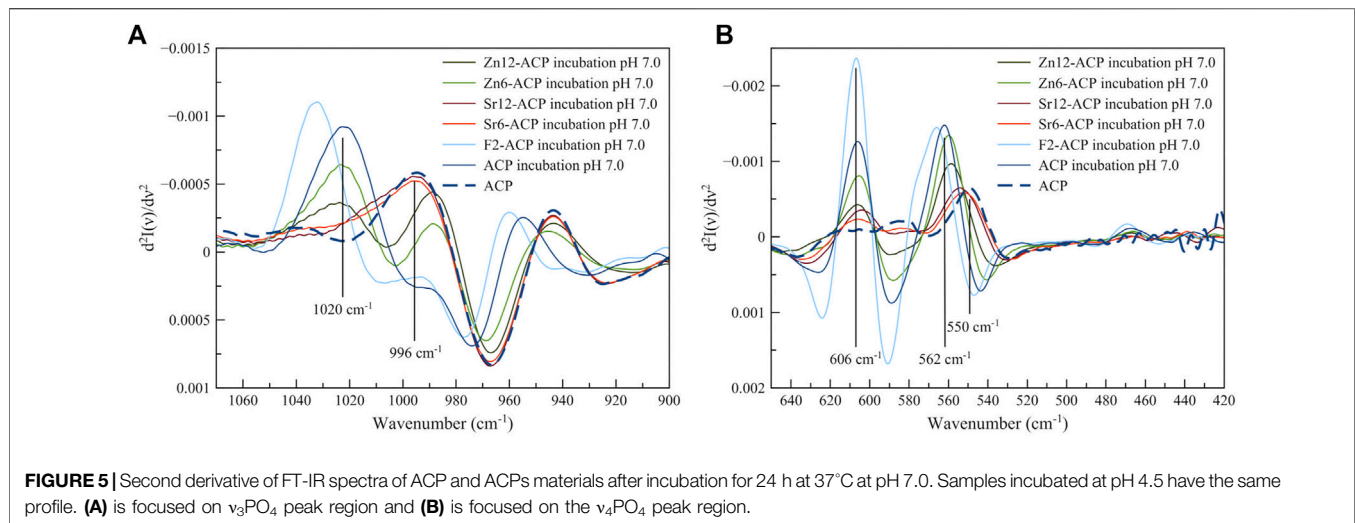
Sample	Slurry pH	Ca^{2+} release (%)	PO_4^{3-} release (%)	F^- release (%)	Sr^{2+} release (%)	Zn^{2+} release (%)
ACP	4.5	5.1 ± 0.2	4.0 ± 0.2	-	-	-
	7.0	1.2 ± 0.2	1.8 ± 0.2	-	-	-
F2-ACP	4.5	5.1 ± 0.1	4.9 ± 0.1	5.1 ± 0.6	-	-
	7.0	4.0 ± 0.2	4.0 ± 0.2	5.8 ± 0.2	-	-
Sr6-ACP	4.5	6.6 ± 0.2	4.2 ± 0.1	-	7.6 ± 0.2	-
	7.0	1.1 ± 0.2	1.4 ± 0.2	-	1.1 ± 0.2	-
Sr12-ACP	4.5	7.0 ± 0.1	6.9 ± 0.2	-	7.4 ± 0.2	-
	7.0	2.3 ± 0.6	3.8 ± 0.9	-	2.5 ± 0.9	-
Zn6-ACP	4.5	5.6 ± 0.8	4.1 ± 0.4	-	-	1.1 ± 0.3
	7.0	0.8 ± 0.4	1.7 ± 0.3	-	-	0.4 ± 0.2
Zn12-ACP	4.5	7.4 ± 0.6	3.7 ± 0.2	-	-	0.5 ± 0.1
	7.0	0.9 ± 0.4	1.7 ± 0.3	-	-	0.2 ± 0.2

FIGURE 4 | (A) PXRD patterns and **(B)** FT-IR spectra of ACPs materials after incubation for 24 h at 37°C at pH 7.0.

literature as it is well known that ACP, similarly to other calcium phosphates, is more soluble at acidic pH than at neutral one (Dorozhkin, 2010). Interestingly, at pH 7.0 the amount of ions released from F2-ACP is higher than the other ACP samples. Considering the ACP samples that have sorted antibacterial effect, both F2-ACP and Sr-ACP have a good F^- or Sr^{2+} release, with ≈5–7% of ions released. On the contrary, Zn-ACP samples have a minimal Zn^{2+} release, with ca. 1% of total zinc released. This reduced Zn^{2+} release could be the cause of the negligible antibacterial activity of Zn-ACP samples despite the presence of Zn-doped HA microcrystallites remineralizing enamel surfaces shown by SEM-EDS analysis. These data suggest that F-ACP and Sr-ACPs dissolve homogeneously within the slurry releasing the antibacterial F^- or Sr^{2+} ions, while upon dissolution of Zn-ACP materials, zinc ions are withheld in the solid phase. This behavior was previously observed for other Zn-doped ACPs, which presented an inferior Zn^{2+} release compared to HA materials (Chen et al., 2012; Schweikle et al., 2019).

However, this phenomenon still has no straightforward interpretation and needs to be investigated in more detail in the future.

After 24 h, the solid residue was studied by PXRD, FT-IR spectroscopy, and SEM-EDS. There is almost no difference between the PXRD patterns and FT-IR spectra of ACPs incubated at pH 7.0 (**Figure 4**) and pH 4.5 (**Supplementary Figures S3A,B**), suggesting that pH did not have a significant influence on the transformation that occurred in the solid phase. Regarding PXRD patterns (**Figure 4A**) after incubation, ACP, F2-ACP, and both Zn-ACP samples show the presence of broad diffraction peaks that were attributed to HA (PDF card number 00-009-0342). The low intensity and high broadness of HA peaks suggest that the material is poorly crystalline. On the other hand, Sr-ACP samples after incubation seem to remain amorphous, but a close examination of PXRD pattern (**Supplementary Figure S3C**) shows a bulging at 31°2θ, which corresponds to the (211) peak of HA. This suggests that also Sr-ACP samples might have a fraction of crystalline phase (see below).

FIGURE 5 | Second derivative of FT-IR spectra of ACP and ACPs materials after incubation for 24 h at 37°C at pH 7.0. Samples incubated at pH 4.5 have the same profile. **(A)** is focused on $\nu_3 PO_4$ peak region and **(B)** is focused on the $\nu_4 PO_4$ peak region.

FT-IR spectra of the samples after slurry incubation (**Figure 4B**) show that Sr-ACPs are similar to the pristine materials, while the $\nu_3 PO_4$ and $\nu_4 PO_4$ bands of ACP, F2-ACP, and both Zn-ACP samples have a different shape. In detail, for these latter materials the IR bands are more resolved and present several peaks at ca. 1,030, 960 cm^{-1}, and at 602 and 562 cm^{-1} which correspond to the $\nu_3 PO_4$, $\nu_1 PO_4$, and $\nu_4 PO_4$ vibrational motions of phosphate ions in HA structure, respectively (Antonakos et al., 2007; Delgado-López et al., 2012), confirming the crystallization to HA. Carbonate and citrate bands are still present in all samples, meaning that these ions were not completely released during ACP dissolution and crystallization. Similarly to the pristine materials, after incubation Sr-ACPs still have more intense citrate and carbonate bands with respect to the other ACPs (**Supplementary Figure S3D**).

To evince the HA content, especially for the Sr-ACP samples, we have used the method developed by Querido et al. (2020) and Uskoković (2020) based on the second derivative of FT-IR spectra. Indeed, the main phosphate IR peaks present a position shift between amorphous and crystalline calcium phosphates that can be highlighted and magnified by calculating the second derivative spectra. The second derivative of FT-IR spectra of incubated ACP samples is reported in **Figure 5** together with the derivative spectra of pristine ACP as a comparison. Regarding the $\nu_3 PO_4$ peak in the 1,100–900 cm^{-1} region (**Figure 5A**), ACP presents a negative peak at ca. 992–996 cm^{-1} while HA has the corresponding peak at 1,016–1,020 cm^{-1} (Querido et al., 2020). The 996 cm^{-1} ACP peak is still present in both Sr-ACP and Zr-ACP samples, while it is absent in ACP and F2-ACP after slurry. On the other hand, all samples show the 1,020 cm^{-1} HA peak, including Sr-ACP ones (as a shoulder). This indicates that incubation has induced the formation of HA in all the materials, although Zn-ACP and Sr-ACP samples still retain an amorphous component. Based on the HA/ACP peaks intensities, the HA content, and crystallinity of the incubated samples can be estimated as F2-ACP > ACP > Zn6-ACP > Zn12-ACP > Sr6-ACP ≈ Sr12-ACP. A similar conclusion can also be drawn from the $\nu_4 PO_4$ peak in the 650–500 cm^{-1} region

(**Figure 5B**). Indeed, ACP presents a negative peak at 545–550 cm^{-1} while in HA the corresponding peak falls at 562 cm^{-1} with an additional peak at 606 cm^{-1} (Uskoković, 2020). In agreement with the observations made for $\nu_3 PO_4$ peak, also in this latter case Zn-ACP and Sr-ACP samples have a contemporary presence of ACP and HA while in ACP sample and F2-ACP only HA is present, with the same order of HA content described above. Overall, this analysis is in agreement with our previous finding that the presence of F- accelerates ACP crystallization kinetics (Iafisco et al., 2018). On the other hand, the presence of Sr^{2+} or Zn^{2+} slows down the crystallization kinetic proportionally to concentration of dopant ion, and Sr^{2+} has a more marked effect than Zn^{2+}. This is in agreement with literature, where is reported that Sr^{2+} or Zn^{2+} ions stabilize ACP and slow down its crystallization in aqueous solution (Root, 1990; Dorozhkin, 2010).

The morphology and composition of ACP samples after incubation as slurry at pH 7.0 is reported in **Supplementary Figure S4** and **Supplementary Table S1**. SEM micrograph of ACP materials (**Supplementary Figure S4A**) shows that the material is still nanostructured and composed of rounded particles with a diameter of ca. 50 nm. This morphology is similar for all the tested ACPs (**Supplementary Figures S4B–F**).

EDS data of dried ACP materials after incubation are in agreement with the previous analysis of remineralized enamel. The amount of Zn was found to be 33% lower than expected in both Zn-ACP compounds, while the Sr and F content was only 10% lower. It has to be noted that EDS can only scan the first micrometer of a compound, therefore there may be substantial differences in the readings between surface composition and bulk composition that may explain these discrepancies.

Overall, our investigation has proved that F- and Sr-doped ACPs partially dissolve and crystallize into HA, releasing F$^-$ or Sr^{2+} ions that can inhibit a cariogenic *S. Mutans* biofilm under conditions that mimic the carious environment. Furthermore, all tested ACPs form a newly formed layer that can remineralize human enamel and, in the case of fluoride, is endowed with an antibacterial effect that could protect enamel from caries. Since in literature is reported that F$^-$ and Sr^{2+} have a synergistic action, it

might be possible that the simultaneous use of F-ACP and Sr-ACP or a co-doped F,Sr-ACP material could have an even stronger antibacterial effect, and this possibility will be investigated in the future.

CONCLUSION

Citrate-stabilized ACP has been successfully doped with fluoride, strontium, or zinc ions. Ion doping did not alter ACP physical-chemical properties but allowed to incorporate up to 2 wt. % F$^-$ and 6–12 wt.% of both Sr^{2+}/Zn^{2+}. Fluoride-doped ACP and strontium-doped ACP were proved to have good antibacterial activity against *S. Mutans* biofilm, with ≈50% inhibition of the viable biomass on contact. This was correlated with an excellent ion release capability that is responsible for the antibiofilm effect. On the other hand, zinc-doped ACP showed poor antibacterial activity, related to shallow release of Zn^{2+} ions in the same timeframe. Our investigation confirmed that all ACP samples release ions and crystallize into HA when in contact with water. The presence of fluoride ions accelerates this crystallization process while zinc and strontium ions decelerate it. Nevertheless, all the ion-doped ACP samples were able to remineralize enamel, showing epitaxial growth of microcristallites especially when the highest amount of Zn and Sr were incorporated into the ACPs. In addition, fluoride incorporated into the remineralized enamel treated with F2-ACP leads to an inhibition of *S. Mutans* viable biomass.

From these results, we proved that citrate-stabilized ACP doped with fluoride or strontium ions is an effective remineralizing material with antibacterial properties. These features suggest that F-ACP and Sr-ACP can be used as multipurpose materials able to treat dental caries by restoring demineralized enamel and inhibiting cariogenic bacteria. Such compounds, therefore, express great potential as advanced materials for oral healthcare. Therefore, future works will be focused on studying the antimicrobial activity of the simultaneous use of F-ACP and Sr-ACP, and on the development of a co-doped F,Sr-ACP material for the treatment of dental caries.

DATA AVAILABILITY STATEMENT

The raw data supporting the conclusions of this article will be made available by the authors, without undue reservation.

AUTHOR CONTRIBUTIONS

All authors have read and agree to the published version of the manuscript. Author Contributions: LDE: conceptualization, investigation, visualization, writing–original draft, writing–review and editing; ACI: investigation, formal analysis, writing–original draft, writing–review and editing; FC: investigation, writing–review and editing; AA: writing–review and editing; EB: writing–review and editing; MI: conceptualization, supervision, writing–original draft, writing–review and editing.

ACKNOWLEDGMENTS

SUPPLEMENTARY MATERIAL

The Supplementary Material for this article can be found online at: https://www.frontiersin.org/articles/10.3389/fmats.2022.846130/full#supplementary-material

REFERENCES

Abou Neel, E. A., Aljabo, A., Strange, A., Ibrahim, S., Coathup, M., Young, A., et al. (2016). Demineralization–remineralization Dynamics in Teeth and Bone. *Int. J. Nanomedicine* 11, 4743–4763. doi:10.2147/ijn.s107624

Addy, M., and Moran, J. (1995). Mechanisms of Stain Formation on Teeth, in Particular Associated with Metal Ions and Antiseptics. *Adv. Dent. Res.* 9 (4), 450–456. doi:10.1177/08959374950090041601

Antonakos, A., Liarokapis, E., and Leventouri, T. (2007). Micro-Raman and FTIR Studies of Synthetic and Natural Apatites. *Biomaterials* 28 (19), 3043–3054. doi:10.1016/j.biomaterials.2007.02.028

Arheiam, A. A., Harris, R. V., and Baker, S. R. (2020). Changes in Dental Caries and Sugar Intake before and during the Conflict in Libya: A Natural experiment. *Community Dent. Oral Epidemiol.* 48 (3), 201–207. doi:10.1111/cdoe.12526

Barbier, O., Arreola-Mendoza, L., and Del Razo, L. M. (2010). Molecular Mechanisms of Fluoride Toxicity. *Chem. Biol. Interactions* 188 (2), 319–333. doi:10.1016/j.cbi.2010.07.011

Blencowe, D. K., and Morby, A. P. (2003). Zn(II) Metabolism in Prokaryotes. *FEMS Microbiol. Rev.* 27 (2-3), 291–311. doi:10.1016/S0168-6445(03)00041-X

Brambilla, E., and Ionescu, A. C. (2021). "Oral Biofilms and Secondary Caries Formation," in *Oral Biofilms and Modern Dental Materials* (Cham, Switzerland: Springer), 19–35. doi:10.1007/978-3-030-67388-8_3

Brauer, D. S., Karpukhina, N., Kedia, G., Bhat, A., Law, R. V., Radecka, I., et al. (2013). Bactericidal Strontium-Releasing Injectable Bone Cements Based on Bioactive Glasses. *J. R. Soc. Interf.* 10 (78), 20120647. doi:10.1098/rsif.2012.0647

Cao, G., Jiang, Y., Chen, F., Lu, B., Tan, S., Feng, V., et al. (2020). Antibacterial Silver-Doped Calcium Phosphate Synthesized by an Enzymatic Strategy for Initial Caries Treatment. *Ceramics Int.* 46 (14), 22466–22473. doi:10.1016/j.ceramint.2020.06.005

Chen, X., Tang, Q.-L., Zhu, Y.-J., Zhu, C.-L., and Feng, X.-P. (2012). Synthesis and Antibacterial Property of Zinc Loaded Hydroxyapatite Nanorods. *Mater. Lett.* 89, 233–235. doi:10.1016/j.matlet.2012.08.115

Chen, L., Suh, B. I., and Yang, J. (2018). Antibacterial Dental Restorative Materials: A Review. *Am. J. Dent.* 31, 6B–12B.

Chernousova, S., and Epple, M. (2013). Silver as Antibacterial Agent: Ion, Nanoparticle, and Metal. *Angew. Chem. Int. Ed.* 52 (6), 1636–1653. doi:10.1002/anie.201205923

Cochrane, N. J., Cai, F., Huq, N. L., Burrow, M. F., and Reynolds, E. C. (2010). New Approaches to Enhanced Remineralization of Tooth Enamel. *J. Dent. Res.* 89 (11), 1187–1197. doi:10.1177/0022034510376046

Combes, C., and Rey, C. (2010). Amorphous Calcium Phosphates: Synthesis, Properties and Uses in Biomaterials. *Acta Biomater.* 6 (9), 3362–3378. doi:10.1016/j.actbio.2010.02.017

Degli Esposti, L., Markovic, S., Ignjatovic, N., Panseri, S., Montesi, M., Adamiano, A., et al. (2021). Thermal Crystallization of Amorphous Calcium Phosphate Combined

with Citrate and Fluoride Doping: a Novel Route to Produce Hydroxyapatite Bioceramics. *J. Mater. Chem. B* 9, 4832. doi:10.1039/D1TB00601K

Delgado-López, J. M., Iafisco, M., Rodríguez, I., Tampieri, A., Prat, M., and Gómez-Morales, J. (2012). Crystallization of Bioinspired Citrate-Functionalized Nanoapatite with Tailored Carbonate Content. *Acta Biomater.* 8 (9), 3491–3499. doi:10.1016/j.actbio.2012.04.046

Dorozhkin, S. V. (2010). Amorphous Calcium (Ortho)phosphates. *Acta Biomater.* 6 (12), 4457–4475. doi:10.1016/j.actbio.2010.06.031

Franci, G., Falanga, A., Galdiero, S., Palomba, L., Rai, M., Morelli, G., et al. (2015). Silver Nanoparticles as Potential Antibacterial Agents. *Molecules* 20 (5), 8856–8874. doi:10.3390/molecules20058856

Godoy-Gallardo, M., Eckhard, U., Delgado, L. M., de Roo Puente, Y. J. D., Hoyos-Nogués, M., Gil, F. J., et al. (2021). Antibacterial Approaches in Tissue Engineering Using Metal Ions and Nanoparticles: From Mechanisms to Applications. *Bioactive Mater.* 6 (12), 4470–4490. doi:10.1016/j.bioactmat.2021.04.033

Hamilton, I. R. (1977). Effects of Fluoride on Enzymatic Regulation of Bacterial Carbohydrate Metabolism. *Caries Res.* 11 (Suppl. 1), 262–291. doi:10.1159/000260304

Helen, S., and Kumar, A. R. (2019). Study of Structural, Mechanical and Dielectric Properties of Ions Doped Apatite for Antibacterial Activity. *Mater. Chem. Phys.* 237, 121867. doi:10.1016/j.matchemphys.2019.121867

Iafisco, M., Ruffini, A., Adamiano, A., Sprio, S., and Tampieri, A. (2014). Biomimetic Magnesium-Carbonate-Apatite Nanocrystals Endowed with Strontium Ions as Anti-osteoporotic Trigger. *Mater. Sci. Eng. C* 35, 212–219. doi:10.1016/j.msec.2013.11.009

Iafisco, M., Degli Esposti, L., Ramírez-Rodríguez, G. B., Carella, F., Gómez-Morales, J., Ionescu, A. C., et al. (2018). Fluoride-doped Amorphous Calcium Phosphate Nanoparticles as a Promising Biomimetic Material for Dental Remineralization. *Sci. Rep.* 8 (1), 17016. doi:10.1038/s41598-018-35254-x

Ionescu, A. C., and Brambilla, E. (2021). "Bioreactors: How to Study Biofilms *In Vitro*," in *Oral Biofilms and Modern Dental Materials: Advances toward Bioactivity* (Cham, Switzerland: Springer Nature), 37. doi:10.1007/978-3-030-67388-8

Ionescu, A. C., Cazzaniga, G., Ottobelli, M., Ferracane, J. L., Paolone, G., and Brambilla, E. (2018). *In Vitro* biofilm Formation on Resin-Based Composites Cured under Different Surface Conditions. *J. Dent.* 77, 78–86. doi:10.1016/j.jdent.2018.07.012

Ionescu, A., Brambilla, E., and Hahnel, S. (2019). Does Recharging Dental Restorative Materials with Fluoride Influence Biofilm Formation? *Dental Mater.* 35 (10), 1450–1463. doi:10.1016/j.dental.2019.07.019

James, S. L., Abate, D., Abate, K. H., Abay, S. M., Abbafati, C., Abbasi, N., et al. (2018). Global, Regional, and National Incidence, Prevalence, and Years Lived with Disability for 354 Diseases and Injuries for 195 Countries and Territories, 1990-2017: a Systematic Analysis for the Global Burden of Disease Study 2017. *Lancet* 392 (10159), 1789–1858. doi:10.1016/S0140-6736(18)32279-7

Kassebaum, N. J., Smith, A. G. C., Bernabé, E., Fleming, T. D., Reynolds, A. E., Vos, T., et al. (2017). Global, Regional, and National Prevalence, Incidence, and Disability-Adjusted Life Years for Oral Conditions for 195 Countries, 1990-2015: A Systematic Analysis for the Global Burden of Diseases, Injuries, and Risk Factors. *J. Dent. Res.* 96 (4), 380–387. doi:10.1177/0022034517693566

Li, Z. Y., Lam, W. M., Yang, C., Xu, B., Ni, G. X., Abbah, S. A., et al. (2007). Chemical Composition, crystal Size and Lattice Structural Changes after Incorporation of Strontium into Biomimetic Apatite. *Biomaterials* 28 (7), 1452–1460. doi:10.1016/j.biomaterials.2006.11.001

Lim, P. N., Chang, L., Tay, B. Y., Guneta, V., Choong, C., Ho, B., et al. (2014). Proposed Mechanism of Antibacterial Action of Chemically Modified Apatite for Reduced Bone Infection. *ACS Appl. Mater. Inter.* 6 (19), 17082–17092. doi:10.1021/am504716g

Limeback, H. (2012). *Comprehensive Preventive Dentistry*. Cham, Switzerland: John Wiley & Sons.

Lynch, R. M., Navada, R., and Walia, R. (2004). Low-levels of Fluoride in Plaque and Saliva and Their Effects on the Demineralisation and Remineralisation of Enamel; Role of Fluoride Toothpastes. *Int. Dent. J.* 54 (S5), 304–309. doi:10.1111/j.1875-595X.2004.tb00003.x

Mao, X., Auer, D. L., Buchalla, W., Hiller, K.-A., Maisch, T., Hellwig, E., et al. (2020). Cetylpyridinium Chloride: Mechanism of Action, Antimicrobial Efficacy in Biofilms, and Potential Risks of Resistance. *Antimicrob. Agents Chemother.* 64 (8), e00576–00520. doi:10.1128/AAC.00576-20

Marsh, P. D., and Zaura, E. (2017). Dental Biofilm: Ecological Interactions in Health and Disease. *J. Clin. Periodontol.* 44, S12–S22. doi:10.1111/jcpe.12679

Miller, S., Truong, T., Heu, R., Stranick, M., Bouchard, D., and Gaffar, A. (1994). Recent Advances in Stannous Fluoride Technology: Antibacterial Efficacy and Mechanism of Action towards Hypersensitivity. *Int. Dent. J.* 44 (1 Suppl. 1), 83–98.

Pace, F., Pallotta, S., Tonini, M., Vakil, N., and Bianchi Porro, G. (2008). Systematic Review: Gastro-Oesophageal Reflux Disease and Dental Lesions. *Aliment. Pharmacol. Ther.* 27 (12), 1179–1186. doi:10.1111/j.1365-2036.2008.03694.x

Posner, A. S., and Betts, F. (1975). Synthetic Amorphous Calcium Phosphate and its Relation to Bone mineral Structure. *Acc. Chem. Res.* 8 (8), 273–281. doi:10.1021/ar50092a003

Querido, W., Shanas, N. a., Bookbinder, S., Oliveira-Nunes, M. C., Krynska, B., and Pleshko, N. (2020). Fourier Transform Infrared Spectroscopy of Developing Bone mineral: From Amorphous Precursor to Mature crystal. *Analyst* 145 (3), 764–776. doi:10.1039/C9AN01588D

Root, M. J. (1990). Inhibition of the Amorphous Calcium Phosphate Phase Transformation Reaction by Polyphosphates and Metal Ions. *Calcif Tissue Int.* 47 (2), 112–116. doi:10.1007/BF02555994

Roveri, N., Battistella, E., Bianchi, C. L., Foltran, I., Foresti, E., Iafisco, M., et al. (2009). Surface Enamel Remineralization: Biomimetic Apatite Nanocrystals and Fluoride Ions Different Effects. *J. Nanomater.* 2009, 1–9. doi:10.1155/2009/746383

Schweikle, M., Bjørnøy, S. H., van Helvoort, A. T. J., Haugen, H. J., Sikorski, P., and Tiainen, H. (2019). Stabilisation of Amorphous Calcium Phosphate in Polyethylene Glycol Hydrogels. *Acta Biomater.* 90, 132–145. doi:10.1016/j.actbio.2019.03.044

Selwitz, R. H., Ismail, A. I., and Pitts, N. B. (2007). Dental Caries. *Lancet* 369 (9555), 51–59. doi:10.1016/S0140-6736(07)60031-2

Tahmassebi, J. F., Duggal, M. S., Malik-Kotru, G., and Curzon, M. E. J. (2006). Soft Drinks and Dental Health: a Review of the Current Literature. *J. Dent.* 34 (1), 2–11. doi:10.1016/j.jdent.2004.11.006

Uskoković, V. (2020). Visualizing Different Crystalline States during the Infrared Imaging of Calcium Phosphates. *Vib. Spectrosc.* 108, 103045. doi:10.1016/j.vibspec.2020.103045

Yang, M., Ren, J., and Zhang, R. (2017). Novel Gallium-Doped Amorphous Calcium Phosphate Nanoparticles: Preparation, Application and Structure Study. *J. Non-Crystal. Sol.* 466-467, 15–20. doi:10.1016/j.jnoncrysol.2017.03.034

Yoon, N. A., and Newman, M. G. (1980). Antimicrobial Effect of Fluorides on Bacteroides Melaninogenicus Subspecies and Bacteroides Asaccharolyticus. *J. Clin. Periodontol.* 7 (6), 489–494. doi:10.1111/j.1600-051X.1980.tb02155.x

Zhao, J., Zhu, Y.-J., Zheng, J.-Q., Chen, F., and Wu, J. (2013). Microwave-assisted Hydrothermal Preparation Using Adenosine 5′-triphosphate Disodium Salt as a Phosphate Source and Characterization of Zinc-Doped Amorphous Calcium Phosphate Mesoporous Microspheres. *Microporous Mesoporous Mater.* 180, 79–85. doi:10.1016/j.micromeso.2013.06.020